Materials Science & Engineering A 875 (2023) 145116

Contents lists available at ScienceDirect

Materials Science & Engineering A

journal homepage: www.elsevier.com/locate/msea

The effect of carbides on the creep performance of Hastelloy X fabricated by laser powder bed fusion

S. Wu [a,b], S.B. Dai [a,b], M. Heilmaier [c], H.Z. Peng [a,b], G.H. Zhang [d], S. Huang [d], X.J. Zhang [d], Y. Tian [a,b,**], Y.M. Zhu [a,b,*], A.J. Huang [a,b]

[a] Monash Centre for Additive Manufacturing, 15-17 Normanby Rd, Notting Hill, VIC, 3168, Australia
[b] Department of Materials Science and Engineering, Monash University, Clayton, VIC, 3800, Australia
[c] Institute for Applied Materials, Karlsruhe Institute of Technology, Engelbert-Arnold-Straße 4, 76131, Karlsruhe, Germany
[d] 3D Printing Research and Engineering Technology Centre, Beijing Institute of Aeronautical Materials, Beijing, 100095, China

ARTICLE INFO

Keywords:
Laser powder bed fusion
Hastelloy X
Creep
Heat treatment
Carbide

ABSTRACT

The creep property is the decisive criterion for the high-temperature application of Hastelloy X (HX alloy) and the carbides have been reported to play an important role in the creep performance of conventionally manufactured HX alloy. However, their impact on the creep performance of HX alloys fabricated by laser powder bed fusion (LPBF) remains to be explored. In this study, two different post-treatments were designed and applied to LPBF HX alloy to create microstructures with different carbide distributions at the grain boundaries (GBs). By systematically comparing grain structures before and after creep, the results revealed that GB sliding was activated at 815 °C, while it is not operative at 650 °C. On this basis, the high amount of GB carbides improved creep lifetime by 2 times at 815 °C via inhibiting GB sliding, while they revealed a negligible impact on creep lifetime at 650 °C. If dislocation-based deformation is operative, the depletion in solutes of the matrix via carbide formation reduces creep resistance unfavourably. These findings provide strategies for further optimization of the creep response of carbide and solid solution strengthened Ni-base alloys.

1. Introduction

The Ni-based superalloy Hastelloy X (HX) has been extensively used in the aerospace industry owing to its excellent corrosion resistance and high-temperature mechanical performance [1–3]. In recent years, laser powder bed fusion (LPBF), a popular additive manufacturing method, has been applied to HX alloy to allow high design freedom and material waste reduction [4–6]. On this basis, the early investigations on the LPBF HX alloys have been focused on the optimization of the processing parameters to obtain crack-free parts [7–16]. Then, the typical microstructure and room-temperature tensile properties of LPBF HX in the as-fabricated and standard heat treated (1175 °C/2 h) conditions were reported [9,17–26]. So far, however, little is known about the high-temperature creep performance of LPBF HX alloy [2,27], which is critical for industrial applications [28–32].

Besides solid-solution strengthening, the microstructure of the HX alloy contains $Cr_{23}C_6$ and Mo_6C carbides for particle strengthening. Compared to conventionally manufactured HX alloy, the carbide number density in the LPBF processed HX alloy is much higher because the rapid cooling process in LPBF leads to a high carbide nucleation rate [25,26,33,34]. In the LPBF fabrication, a hot isostatic pressing (HIP) process is usually applied to the components to decrease the printing-induced defects. Nevertheless, numerous carbides were also observed after the standard HIP treatment (1175 °C/2 h, 150 MPa) [18,25]. If these carbides decorate the grain boundary (GB) to a large extent, it is assumed commonly that they inhibit GB sliding during creep at relatively high service temperatures, i.e. over 800 °C [35–42]. Hence, the GB carbides are expected to improve the creep resistance. By contrast, some studies have shown that GB sliding is not operative at medium-high temperatures, such as 650 °C [28,43–45]. For instance, there was no apparent difference in creep lifetime at 650 °C when the grains had grown from about 80 μm to 280 μm in the LPBF Inconel 718 [46]. Thus, it appears that the effect of carbides in pinning GBs will be minimal in such conditions. In addition, it has been observed that the GB carbides are prone to crack initiation under loading, resulting in an accelerated creep rupture [28,31]. Moreover, extensive precipitation of

* Corresponding author. Monash Centre for Additive Manufacturing, 15-17 Normanby Rd, Notting Hill, VIC, 3168, Australia.
** Corresponding author. Monash Centre for Additive Manufacturing, 15-17 Normanby Rd, Notting Hill, VIC, 3168, Australia.
E-mail addresses: yang.tian@monash.edu (Y. Tian), yuman.zhu@monash.edu (Y.M. Zhu).

https://doi.org/10.1016/j.msea.2023.145116
Received 16 March 2023; Received in revised form 20 April 2023; Accepted 2 May 2023
Available online 2 May 2023

Mo_6C and $Cr_{23}C_6$ carbides in the HX alloy will deplete the solid solution strengthening elements in the matrix, which may lead to reduced creep resistance.

From the above-mentioned issues, it becomes clear that carbides play an important role in the creep properties of LPBF HX alloy. In particular, their role at various creep temperatures remains an unclear and open issue requiring a comprehensive study on the subject. In pursuit of targeting optimal creep performance for a wide range of temperatures for the LPBF HX alloy, this study designed two post-treatment schemes for LPBF HX alloy to create different carbide distributions. The creep properties of these differently treated HX alloys were investigated at 650 °C and 815 °C for selected applied stresses and the corresponding microstructure evolution during creep was characterised. To quantitatively describe the temperature-dependent effects of carbides on the creep properties at different conditions, the degree of GB sliding was estimated through a simplified model. To this end, the findings in this study are expected to provide a pathway to improve the creep performance of LPBF HX alloy through the control of carbides precipitation and distribution in the microstructure.

2. Experimental procedure

2.1. Materials and LPBF process

The gas-atomized HX powder was supplied by HFYC (ZHENJIANG) SUPERALLOY CO.LTD. The powder composition is shown in Table 1 (supplier specification). The powder was sieved by a 53 μm siever before the LPBF process. The powder size distribution is shown in Table 2, where more than 90% powders have their diameters (D_{90}) smaller than 52.9 μm. The virgin powder was used in this study. The LPBF machine used in this study was EOSM290. The LPBF process was performed using the following parameters: laser power of 285 W, scan speed of 960 mm/s, hatch distance of 0.11 mm, layer thickness of 0.04 mm, preheating temperature of 100 °C and alternating scanning strategy.

2.2. Post heat treatments/HIP

Post heat treatment of the as-fabricated HX was performed in a TF1700 tube furnace with a maximum working temperature of 1700 °C under argon protection. The temperature accuracy was controlled within the range of ±10 °C by a Type-B thermocouple and validated by a Type-K thermocouple. The HIP was performed in an Avure QIH-9 device. The heat treatment/HIP routes are listed in Table 3.

2.3. Mechanical testing

After heat treatment, the CNC machine tool was applied for specimen machining and surface polishing. The hexagonal prisms were machined to the specimen geometry with a gauge length of 20 mm and a gauge diameter of 5 mm. Then, the specimen surfaces were ground and longitudinally polished. This process was performed following ASTM-E139 standard. Fig. 1 shows a schematic of creep specimen and corresponding building and loading directions. The HX alloy samples after heat treatment were then surface polished and tested on a GNCJ-100E creep testing machine with a maximum load capacity of 100 kN. An extensometer was attached to the gauge section in creep bars to measure creep strain continuously during the tests. The creep tests were conducted at 650 °C and constant load 340 MPa, and 815 °C and 105 MPa, respectively. The creep tests were performed under constant stress. The temperature was monitored by a centrally located multi-screen monitoring system, with readings up to 120 times per hour. Two creep specimens were used for each condition. The high temperature tensile tests were conducted at 815 °C. The deformation rate before yield was 0.005 mm/min and increased to 2 mm/min after yielding, with an original gauge length of 30 mm and gauge diameter of 6 mm (diameter) in accordance with the ASTM E21-20 standard. This corresponds to strain rates of 2.8×10^{-6} s^{-1} and 1.1×10^{-5} s^{-1} before and after yielding, respectively.

Table 1
Chemical composition of HX alloy powder.

Element	Ni	Cr	Fe	Mo	Co	C	Si	Mn
Content (wt. %)	48.65	21.50	19.27	8.86	1.58	0.06	0.07	0.01

Table 2
Powder size distribution.

D_{10}	D_{50}	D_{90}
18.7 μm	31.8 μm	52.9 μm

Table 3
Post heat treatment/HIP routes for LPBF HX.

Designation	Heat treatment route
HIP	1230 °C × 150 MPa × 2 h + FC (~4 °C/min)
HIPHT	1230 °C × 150 MPa × 2 h + FC (~4 °C/min) + 1230 °C × 2 h + AC

Note: FC and AC stands for furnace cooling and air cooling, respectively.

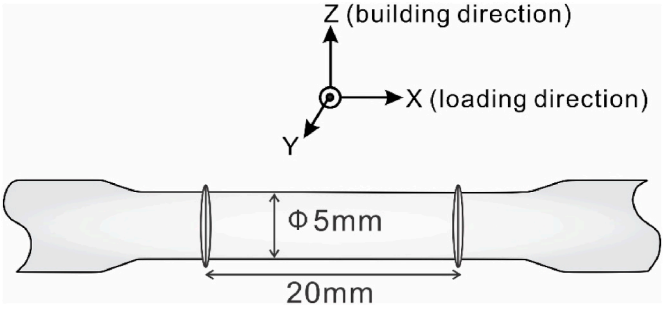

Fig. 1. A schematic diagram showing the creep specimen relative to building and loading directions.

2.4. Microstructure characterization

The heat-treated HX samples before and after creep testing were prepared for microscopic characterization. For scanning electron microscopy (SEM) observations, the samples or creep bars were cut by a Secotom-15 along, or perpendicular, to the build direction. The sliced specimens were then hot-mounted and ground by abrasive papers from 320 to 1200 grit. After that, sample polishing was conducted using a Struers Tegramin-30 Polishing System. A JEOL-7001F field emission scanning electron microscope, equipped with backscatter electron (BSE) and electron backscatter diffraction (EBSD) detectors, was used to examine the samples. The BSE images were obtained under an accelerating voltage of 15 kV and a working distance of 10.0 mm. The EBSD images were taken with an accelerating voltage of 20 kV and a step size of 1.5 μm.

3. Results

To explore the influence of carbides on the high-temperature mechanical properties, the aforementioned post heat treatment routes were applied to as-fabricated LPBF HX to generate microstructures with different carbide distributions. Then, the microstructures (e.g., carbides and grain structure) under different heat treatment schemes were examined and compared. To understand the influence of carbides on GB sliding at different creep conditions, the grain structures after creep were analysed.

3.1. Carbides

Fig. 2 shows the phase fraction diagram of the HX alloy calculated by ThermoCalc with the database TCNI8. According to this, only a face-centred cubic (fcc) γ matrix exists when the temperature decreases from 1320 °C to 1170 °C. As temperature further decreases, Mo_6C will be formed in the range from 1170 °C to 900 °C, while $Cr_{23}C_6$ will be formed between 940 °C and 500 °C.

As-fabricated HX was subjected to two sets of post treatment (HIP, HIPHT as listed in Table 3) and the resulting microstructures are displayed in Figs. 3 and 4, respectively. From the BSE image in Fig. 3a, it has to be noted that a high density of grey particles, with a size of around 1 μm, exists after HIP. Apart from these grey particles, a few small white particles (at a much smaller size of ~0.1 μm) can also be observed along GBs. In contrast, only a few white particles exist in the microstructure of the HIPHT condition, as shown in Fig. 3b. SEM-EDS was used to identify these particles, with the results summarized in Table 4, where the large grey particles are Cr-enriched with a Cr concentration of ~60%. The concentrations of Ni and Fe in the grey particles are only ~8% and 6%, respectively, both of which are much lower than their content in the bulk HX alloy, being ~48% and 19%, respectively. In contrast, the Ni and Fe concentrations in the small white particles, as indicated by "particle 2" in Fig. 3 and Table 4, respectively, are much higher than measured in the grey "particle 1", but still lower than that of bulk HX alloy. The Cr content in "particle 2" (~18%) is much lower than in the bulk HX alloy, indicating the white particles do not match with the $Cr_{23}C_6$ carbide. To this end, the Mo-enrichment in "particle 2" (~25%), compared to ~8% in bulk HX alloy, indicates the formation of a Mo-rich M_6C-type carbide.

The composition of the matrix through HIP and HIPHT processing was determined by more than 10 EDS tests, the average values are given in rows matrix 1 and matrix 2 in Table 4, respectively. It can be seen that the Ni and Fe contents of matrix 2 are slightly lower than those of matrix 1, while the Cr and Mo contents are higher. This is attributed to the Mo and Cr-rich particles forming at GBs after the HIP treatment, leading to the depletion of Mo and Cr in matrix 1.

3.2. Grain structure

As shown above, there are numerous carbides formed in HIP condition while no carbides can be found in HIPHT condition. Then, another creep-related microstructural factor, namely the grain structure, was characterized prior to the creep tests. Fig. 4a and b display IPF maps of LPBF HX alloy before creep along the XZ plane after HIP and HIPHT, respectively, with Z being the built direction in all cases. The grain structure in both conditions appears equiaxed and there is no obvious difference between the two conditions in terms of morphology and size. However, this is different from the LPBF HX alloy under conventional heat treatment (1175 °C/2 h), for which the as-built columnar grain structure was maintained [26]. Also, the corresponding geometry necessary dislocation (GND) map in Fig. 4c and d, show comparably low dislocation densities due to the grain recrystallisation which took place at 1230 °C. The grain size distribution and average grain size were obtained by measuring more than 1000 grains for each condition. In both conditions, the majority of the grains were between 30 and 80 μm in size, with only a few exceeding 120 μm, Fig. 4e and f. The area-average spherical-equivalent grain sizes are 67 μm and 70 μm for HIP and HIPHT conditions, respectively.

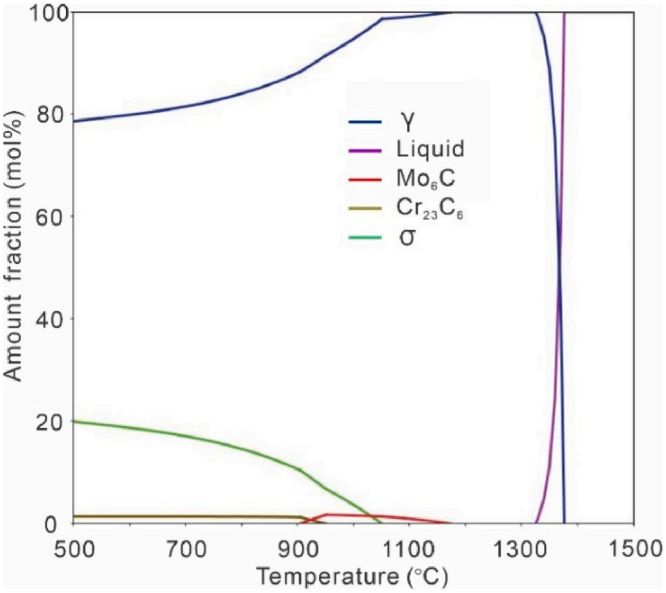

Fig. 2. Calculated phase fraction versus temperature for HX alloy.

3.3. Mechanical properties

To understand the influence of carbides (and ensuing microstructure) on the creep performance at different temperatures, two creep tests were performed under each condition at 815 °C and 650 °C. The corresponding results are shown in Fig. 5. Fig. 5a-b represents creep curves at 650 °C (340 MPa) and 815 °C (105 MPa), respectively. The creep lifetime and steady-state creep rate at different conditions are summarized in Fig. 5(c and d). At 815 °C, the creep lifetime (43.2 h) of HX after HIP is about 2 times longer than after HIPHT (23.8 h), although the steady state creep rate for the HIP (6.7×10^{-7}/s) condition is higher than after HIPHT (4.0×10^{-7}/s). For 650 °C, the difference in creep lifetime between HIP (34.5 h) and HIPHT (36.5 h) is much smaller than for 815 °C, i.e., 34.5 h vs. 36.5 h, respectively, however, the steady-state creep rate of HX after HIP (9.7×10^{-7}/s) is also higher than after HIPHT (2.9×10^{-7}/s). The higher creep rates for the HIP condition than after HIPHT at both 650 °C and 815 °C indicate a lower resistance to dislocation motion. This is supported by the high-temperature tensile curves after HIP and HIPHT conditions at 815 °C, presented in Fig. 6, which yield a lower yield stress for the HIP condition (142 MPa) as compared with HIPHT (165 MPa).

3.4. Microstructure after creep

The grain structure evolution during creep may give hints on the acting creep deformation mechanism, in other words, grains will tend to retain their original shape during GB sliding, whereas grains may stretch along the loading direction when the deformation occurs by dislocation motion [39,40,47–49]. Therefore, to elucidate the main acting deformation mechanism during creep, the grain structures after creep were quantitatively characterised. Fig. 7(a and b) shows the IPF maps of the HX alloy in the HIP condition while Fig. 7(c and d) shows those of HX for HIPHT at 650 °C and 815 °C, respectively. As displayed in Fig. 7(a) and (c), grain elongation along the loading direction appears to be obvious at 650 °C for both, HIP and HIPHT samples. In contrast, the grains maintained the original equiaxed structure at the creep temperature of 815 °C, (Fig. 7(b) and (d)). To quantitatively, describe the grain structure change during creep, the grain aspect ratio (GAR) was calculated as the grain length along the loading direction divided by the grain width perpendicular to the loading direction, similar to the approach taken in the literature on creep of ODS Ni-base alloys [50]. The average GAR of HX alloy before creep was measured as 1.00–1.01. The average GAR of the HX alloy under HIP and HIPHT after 650 °C creep has evolved to 1.58 (Fig. 8a) and 1.36 (Fig. 8c) for both heat treatment conditions, thus being significantly greater than unity, further confirming the elongation of the grain structure. In contrast, the GAR after 815 °C creep is generally much smaller than after 650 °C creep, see Fig. 8b and d, respectively. In particular, for the grain structure of specimens after

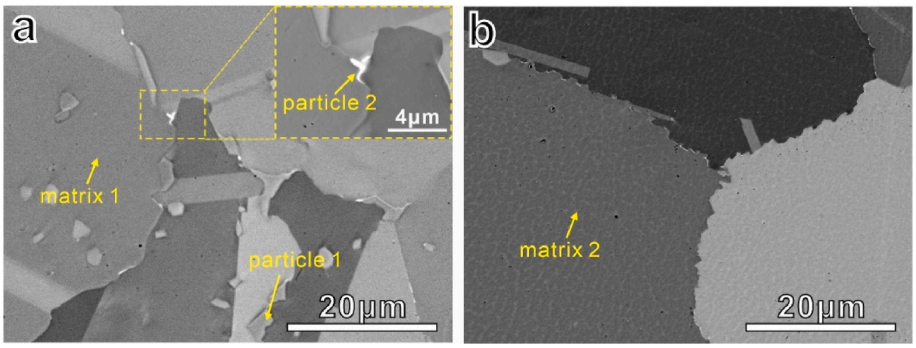

Fig. 3. SEM micrographs showing carbide distribution for (a) HIP and (b) HIPHT conditions. The composition of two types of carbides with different contrast (shown by arrow 1 and arrow 2) and of the matrix was identified by ten EDS point analyses each (Table 2).

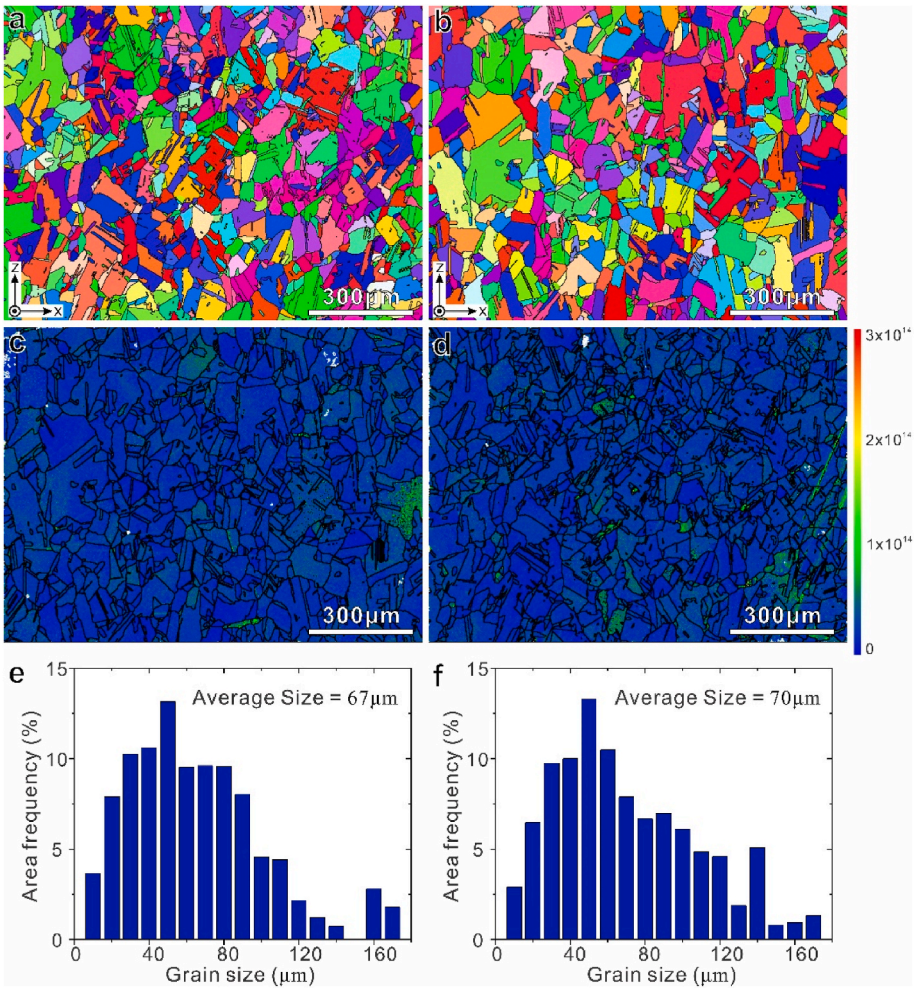

Fig. 4. EBSD maps of the LPBF HX alloy showing the XZ plane grain structure for (a) HIP and (b) HIPHT, where Z is the build direction. (c–d) Corresponding GND density map along the XZ plane in (a) and (b) respectively. (e–f) Grain size distribution in (a) and (b), respectively. Only grains with misorientation >10° were counted as an established criterion for high-angle grain boundaries (HAGB).

Table 4
EDS point analysis results corresponding to the spots indicated in Fig. 2.

EDS points	Ni-wt%	Cr-wt%	Fe-wt%	Mo-wt%	Co-wt%
Particle 1	8.3 ± 1.0	62.7 ± 1.3	6.5 ± 0.4	22.0 ± 0.1	0.5 ± 0.1
Particle 2	39.3 ± 0.1	18.5 ± 0.1	14.9 ± 0.4	25.7 ± 0.4	1.7 ± 0.1
Matrix 1	50.5 ± 0.9	20.2 ± 0.5	18.8 ± 0.3	9.0 ± 0.3	1.6 ± 0.2
Matrix 2	48.6 ± 0.4	22.0 ± 0.2	18.2 ± 0.2	9.6 ± 0.2	1.7 ± 0.2

HIPHT treatment and after 815 °C creep, the GAR of 1.04 is still very close to equiaxed, implying that GB sliding may be the dominant deformation mechanism for this microstructure.

Fig. 9 shows the SEM images after 815 °C creep test. In the GB regions without carbides (marked by red arrows), the GBs were relatively smooth, due to the free GB sliding during creep. In contrast, the GBs with carbides (marked by yellow arrows) show serrated structure, indicating they were restricted by the carbides during the creep and thus not compatible with the adjacent boundaries.

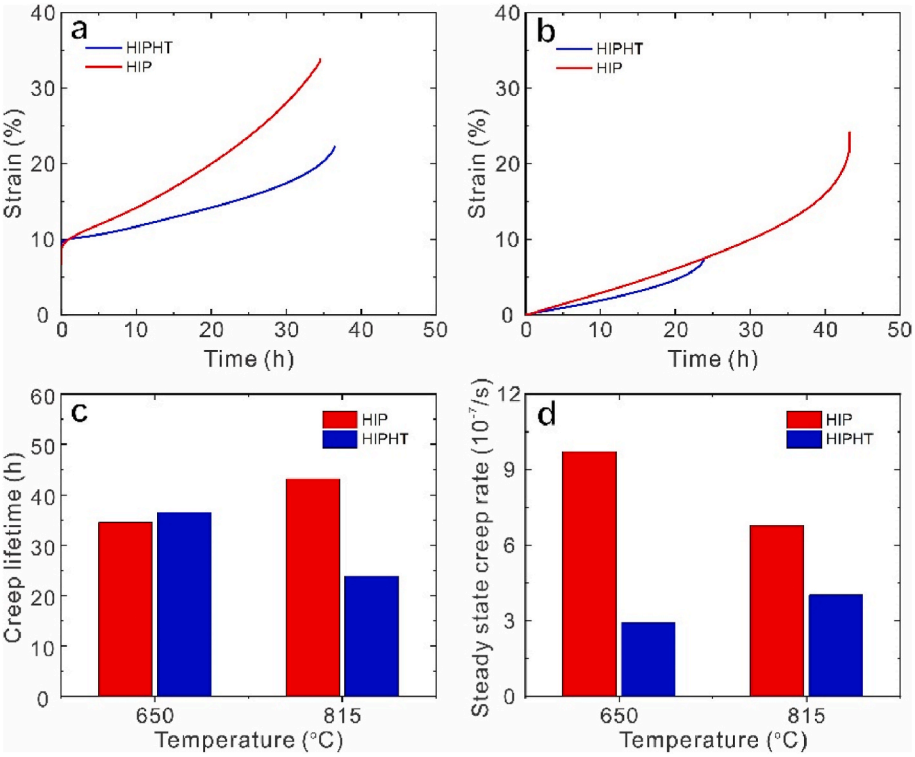

Fig. 5. Creep curves for heat-treated LPBF HX alloy at testing conditions of (a) 650 °C/340 MPa and (b) 815 °C/105 MPa. Comparison of (c) creep lifetime and (d) steady-state creep rate, which is determined as the minimal value of slope in creep vs time curves displayed in (a) and (b) for HIP (red) and HIPHT (blue) conditions, respectively. Note the large initial strain of around 10% of the creep curves, which is due to the creep stress of 340 MPa exceeding the yield strength of the alloys at 650 °C. (For interpretation of the references to colour in this figure legend, the reader is referred to the Web version of this article.)

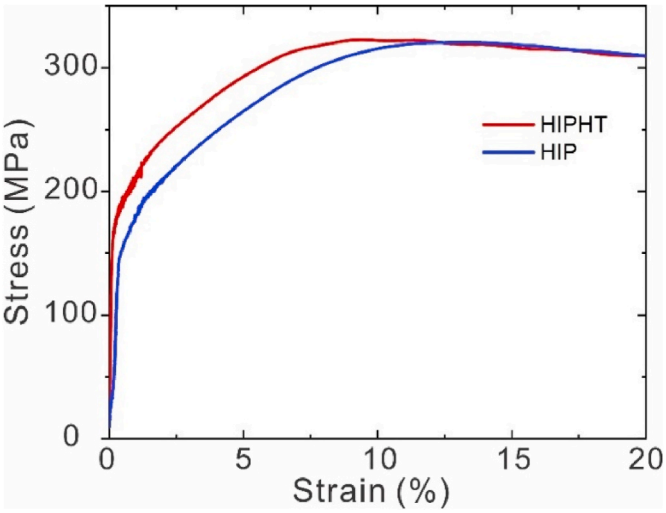

Fig. 6. Cut-out of tensile curves for heat-treated LPBF HX alloy at a temperature of 815 °C, elongation to failure was greater than 60% for both conditions.

4. Discussion

The temperature-dependent effects of carbides on the creep performance of LPBF HX alloy were attributed to the temperature-dependent creep deformation mechanism. At homologous temperatures (i.e., T/T_m, T is the testing temperature and T_m is the melting temperature) higher than about 0.5, one recognizes three possible contributions to creep, depending on stress level and temperature: (a) dislocation motion by glide and climb inside the matrix, (b) GB sliding accommodated by either (volume or GB) diffusion or dislocation motion, (c) diffusional creep [51]. The mechanism which leads to the highest deformation rate at a certain temperature and stress regime would dominate creep deformation whilst the others are then usually considered negligible. At the creep temperature where GB sliding is operative, if the GB sliding cannot be accommodated by either dislocation motion inside the matrix or by volume or GB diffusion, cavities or creep cracks will form, leading to creep fracture. One proper and commonly accepted method to inhibit GB sliding is to decorate them with (carbide) particles and, therefore, they could promote longer creep lifetime. However, at a medium-high temperature, the dislocation-motion is the main creep deformation mode, and the GB sliding usually becomes negligible. In this case, the creep cracking originates from dislocation pile-up against GB particles. Assuming this mechanism to be operative, GB carbides would not lead to improved creep lifetime by controlling GB sliding. Consequently, the steady state creep rate then represents the resistance to dislocation motion. In the specific case of the HX alloy, excessive carbide formation at the GB reduces solid-solution strengthening by depletion of the matrix in Cr and Mo and, therefore, eventually leads to a higher creep rate (i.e., less creep deformation resistance). Therefore, in the following section, the contribution of GB sliding to creep deformation at a different temperature will be estimated first to shed light on the dominant creep deformation mechanism. Subsequently, a strategy to optimise the creep performance of LPBF HX alloy at different creep temperatures by tailoring carbide formation will be discussed.

As discussed above, if GB sliding is activated at certain creep conditions, more carbide pinning of GBs may contribute to a longer creep lifetime. To understand the influence of carbides on GB sliding and, therefore, the creep lifetime, the degree of GB sliding at each condition has to be analysed.

The degree of GB sliding can be estimated by comparing the grain structure, i.e., grain aspect ratio, before and after creep [39,48,52]. As shown in the schematic Fig. 10, if there is no GB sliding ($C_{gbs} = 0$, top right), the grain will be elongated along the loading direction (horizontal in Fig. 10). By contrast, assuming only GBS to be operative ($C_{gbs} = 1$), grain shape remains equiaxed (lower right in Fig. 10). If there is only plastic deformation, the bulk volume will not change during the deformation process. On this basis, for a grain structure with an initial grain aspect ratio GAR_0, grain length l_0, width w_0 and a uniaxial strain ε, the initial grain aspect ratio GAR_0 is:

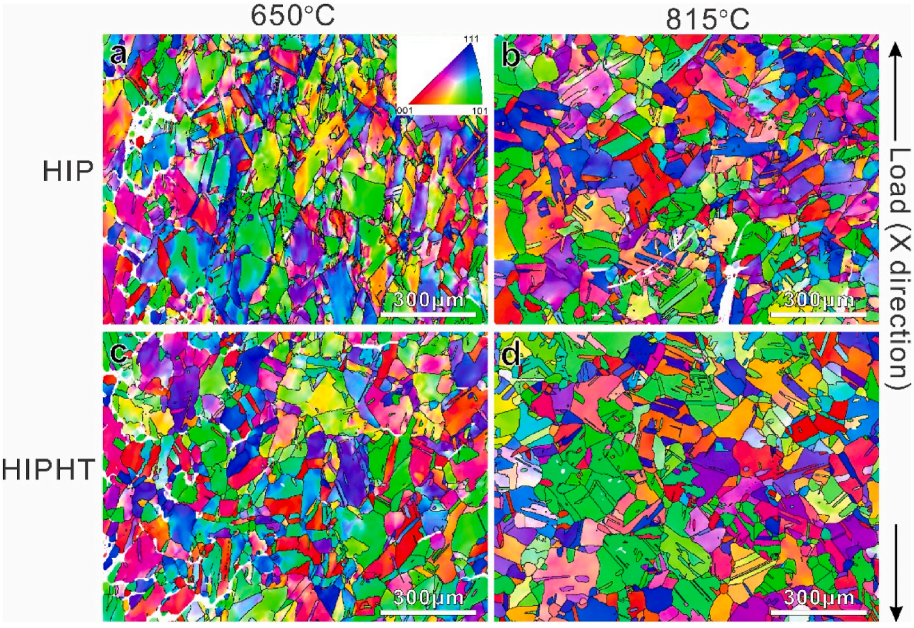

Fig. 7. Grain structure of HX alloy under the post treatment of (a) HIP (b) HIPHT after 650 °C creep tests and (c) HIP (d) HIPHT after 815 °C creep tests.

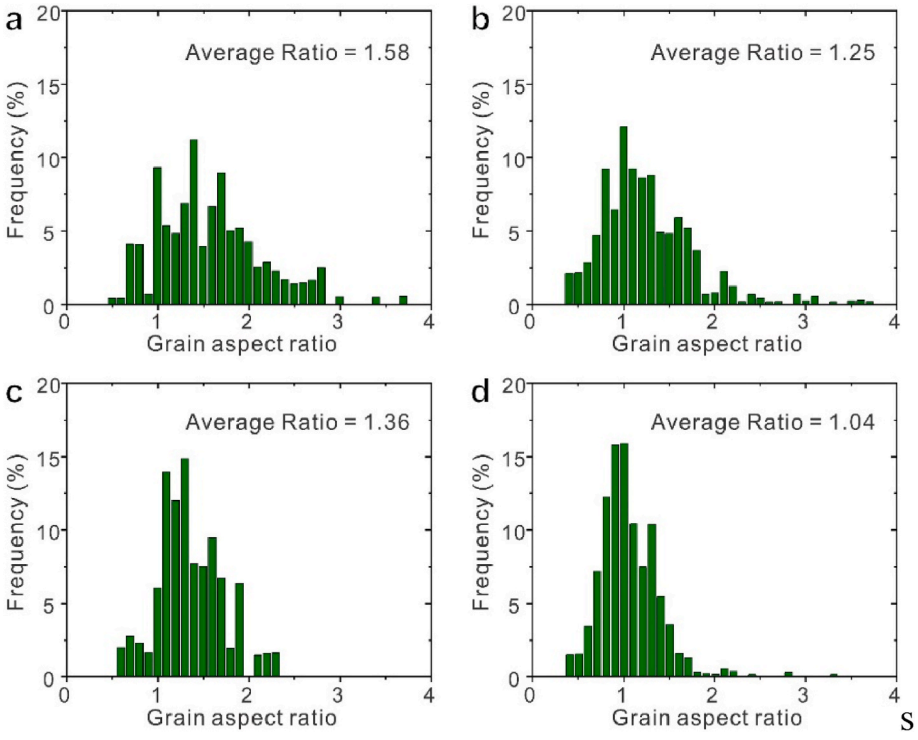

Fig. 8. Measured grain aspect ratio of HX alloy under the post treatment of (a) HIP (strain to failure: 35%) (c) HIPHT (22%) after 650 °C creep tests and (b) HIP (24%) (d) HIPHT (8%) after 815 °C creep tests.

$$GAR_0 = \frac{l_0}{w_0} \tag{1}$$

For a uniaxial strain, ε, the overall deformation is composed of dislocation motion ε_{dis} inside the matrix and GB sliding ε_{gbs}:

$$\varepsilon = \varepsilon_{dis} + \varepsilon_{gbs} \tag{2}$$

For deformation without GB sliding ($\varepsilon = \varepsilon_{dis}$), the grain size l_1 along the loading direction becomes:

$$l_1 = l_0 \times (1 + \varepsilon) \tag{3}$$

while the grain size w_1 perpendicular to the loading direction becomes:

$$w_1 = w_0 \times (1 + \varepsilon)^{-0.5} \tag{4}$$

With the plausible assumption that each grain is uniformly deformed, then the calculated grain aspect ratio (CGAR) after deformation is:

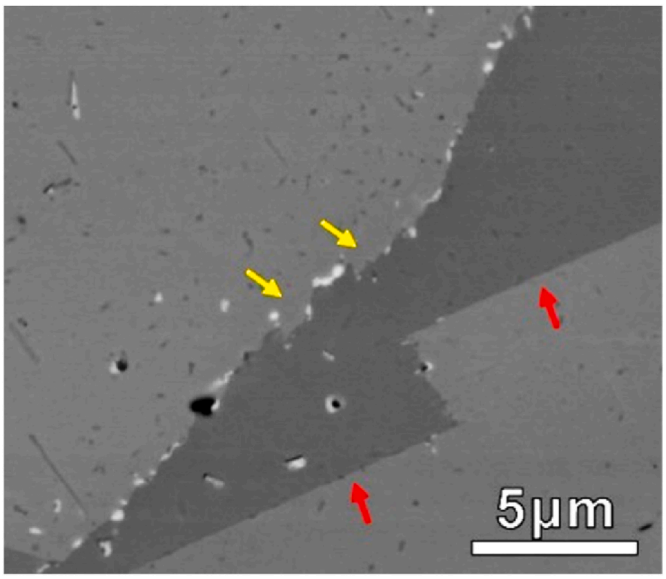

Fig. 9. SEM micrographs of HX alloy under HIP condition after 815 °C creep test. The yellow arrows show the serrated GBs, which indicates the pinning effect of carbides on GB sliding. The red arrows show smooth GBs, where few carbides exist. (For interpretation of the references to colour in this figure legend, the reader is referred to the Web version of this article.)

$$CGAR = GAR_0 \times (1+\varepsilon)^{1.5} \quad (5)$$

In the experiment, since all high-temperature deformations mechanisms operate simultaneously, GB sliding will also contribute to the deformation but will not affect the grain structure. On this basis, the change in grain shape is considered to be caused exclusively by dislocation motion. The experimental grain aspect ratio (EGAR) can then be calculated as:

$$EGAR = GAR_0 \times (1+\varepsilon_{dis})^{1.5} \quad (5)$$

The contribution of GB sliding (C_{gbs}) to the total deformation can be estimated as:

$$C_{gbs} = \frac{\varepsilon_{gbs}}{\varepsilon} = 1 - \frac{\varepsilon_{dis}}{\varepsilon} = 1 - \frac{\left(\frac{EGAR}{GAR_0}\right)^{\frac{2}{3}} - 1}{\varepsilon} \quad (6)$$

In this work, the initial grains were equiaxed (Fig. 4) and the GAR_0 is taken as 1. If there is no GB sliding, the magnitude of EGAR is close to CGAR (e.g., $(1+\varepsilon)^{1.5}$). In contrast, the grains tend to keep their original shape if GB sliding is active. In other words, with GB sliding, the value of EGAR should be smaller than CGAR and closer to GAR_0.

To estimate the degree of GB sliding during creep, the EGAR, CGAR and estimated contributions from GBS to creep deformation under different conditions are compared in Fig. 11. As shown in Fig. 7a-c, obviously significant grain elongation occurs along the loading direction at 650 °C for both HIP and HIPHT conditions, respectively. The average grain aspect ratio of HIP (1.58) is larger than HIPHT (1.36) at 650 °C, which is due to the larger elongation to failure (35% vs. 22%). The measured EGAR after creep for the HIP and HIPHT conditions at 650 °C is consistent with the calculated value CGAR, indicating that the contribution from GB sliding is negligible. Consequently, the estimated C_{gbs} of HIP and HIPHT at 650 °C are close to 0%.

For 815 °C, the grain structure, especially for the HIPHT condition (EGAR~1.04, Fig. 7d), remains relatively equiaxed. This is believed to be caused by a more substantial contribution of GB sliding to the overall creep deformation at the higher temperature, and consequently, the grains tend to keep their original shape and change their positions with respect to each other to accommodate the specimen deformation. The calculated C_{gbs} of HIP (33%) is much lower than that of HIPHT (67%) at 815 °C. This result can be easily rationalized by the fact that there are more carbides decorating the GBs for the HIP than for the HIPHT condition, hence, effectively suppressing GB sliding during creep.

In short, a higher fraction of carbides hinders more effectively GB sliding at 815 °C and, consequently, leads to a longer creep lifetime. By contrast, at 650 °C, the GB carbides have only minor influences on the creep lifetime due to negligible contributions from GB sliding to overall creep.

In addition to creep lifetime, steady state creep rate reflects the

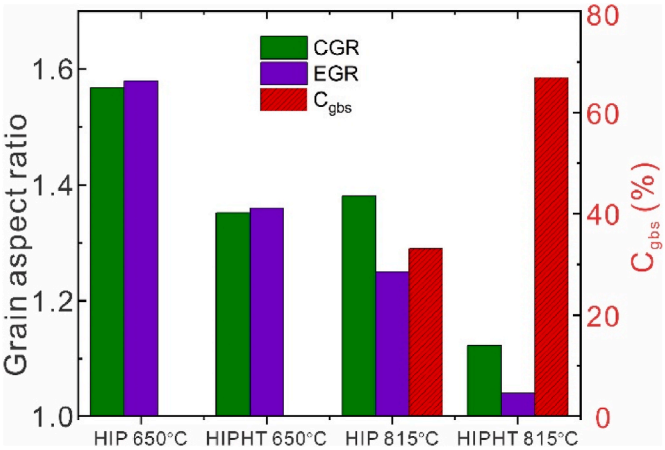

Fig. 11. Comparison between experimentally measured grain aspect ratio, calculated grain aspect ratio and estimated contribution from GB sliding to creep deformation for the HX alloy after HIP and HIPHT for 650 °C and 815 °C creep. Note that at 650 °C the calculated contribution from GB sliding is close to zero.

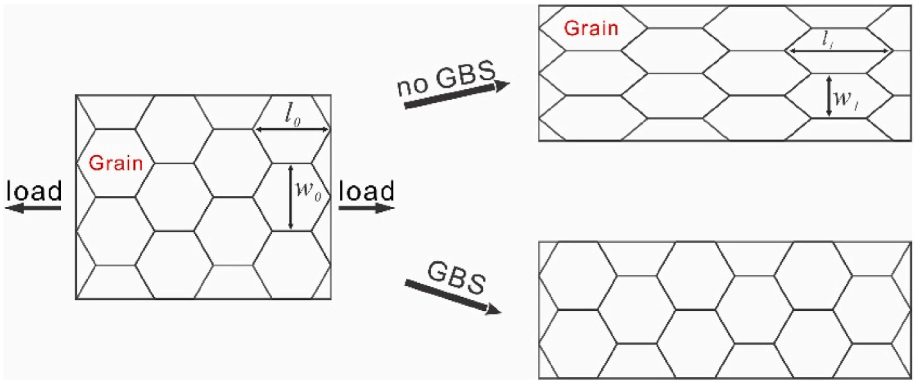

Fig. 10. Schematic of grain structure evolution during creep in the condition of (a) no GB sliding (b) GB sliding.

resistance to creep deformation. In application, a component with a low steady-state creep rate is desirable because it maintains high dimensional accuracy during the deformation process. The results in this study show that the HIP condition always reveals a higher steady state creep rate than the HIPHT condition at both, 650 °C (9.7×10^{-7}/s vs. 2.9×10^{-7}/s) and 815 °C (6.7×10^{-7}/s vs. 4.0×10^{-7}/s). As Hastelloy X is a solid-solution strengthened alloy, the deformation resistance in the grain interior is mainly attributed to the amount of elements in the solid solution. In the LPBF HX alloy after HIP, there exists a high density of $Cr_{23}C_6$ and Mo_6C carbides, which are predominantly located at the GBs, and, therefore, the Cr and Mo concentration inside the matrix is reduced. Table 4 displays that the total Cr and Mo concentration of the matrix after HIP is 2–3% lower than after HIPHT, leading to reduced solid solution strengthening and deformation resistance of HIP condition. This is at least qualitatively confirmed by the yield strength of HIP (142 MPa) treated HX alloy, which is also lower by about 20 MPa than that of HIPHT (165 MPa) at 815 °C, Fig. 6.

5. Conclusion

In this work, the focus was laid on carbide distribution in Hastelloy X (HX) alloy produced by LPBF for studying the impact on creep performance at medium-high (650 °C) to high (815 °C) temperatures. Two post treatments, HIP (high carbide density) and HIPHT (only a few carbides), were designed to produce seemingly different carbide distributions in the microstructure. The creep performance and grain structure evolution during the creep of HX alloys via both post treatments were studied at 650 °C and 815 °C to determine the temperature-dependent effects of the carbides. The main conclusions can be summarized as follows:

1. Carbides are desired for the creep of LPBF HX alloy at 815 °C and the results in this study showed that the presence of carbides at the GBs can significantly increase the creep lifetime from 23.8 h (HIPHT) to 43.2 h (HIP). However, no obvious difference was found in creep lifetime between the HIP and HIPHT conditions at 650 °C.
2. The contribution of GB sliding (C_{gbs}) was analysed to interpret the temperature-dependent effects of carbides on creep performance. At 650 °C, the C_{gbs} are around 0% for both HIP and HIPHT, indicating negligible GB sliding. Hence, the existence of carbides has only little influence on creep lifetime at 650 °C. In contrast, at 850 °C the C_{gbs} increased to 34% and 67% for HIP and HIPHT conditions, respectively. Since the C_{gbs} for HIP is significantly lower than for HIPHT due to the high carbide density of the former, the creep lifetime of HIP is longer than that of HIPHT condition.
3. The formation of a higher amount of carbides leads to a depletion of the matrix in strengthening solutes and, therefore, reduces the resistance for dislocation motion in HIP conditions. Consequently, the steady state creep deformation rate of HIP is higher than HIPHT at both 650 °C (9.7×10^{-7}/s vs. 2.9×10^{-7}/s) and 815 °C (6.7×10^{-7}/s vs. 4.0×10^{-7}/s). By contrast, the carbides have little impact on the creep lifetime at 650 °C. Therefore, post-treatments are recommended that produce fewer carbides in HX alloy, if applications at only medium-high temperatures around 650 °C are anticipated.

CRediT authorship contribution statement

S. Wu: Methodology, Formal analysis, Investigation, Writing – original draft. **S.B. Dai:** Formal analysis, Investigation. **M. Heilmaier:** Validation, Writing – review & editing. **H.Z. Peng:** Investigation. **G.H. Zhang:** Methodology, Validation. **S. Huang:** Methodology, Validation. **X.J. Zhang:** Methodology, Validation. **Y. Tian:** Conceptualization, Supervision, Project administration, Writing – review & editing. **Y.M. Zhu:** Conceptualization, Supervision, Validation, Writing – review & editing. **A.J. Huang:** Conceptualization, Supervision, Funding acquisition.

Declaration of competing interest

The authors declare that they have no known competing financial interests or personal relationships that could have appeared to influence the work reported in this paper.

Data availability

Data will be made available on request.

Acknowledgements

The authors gratefully acknowledge the funding support from AmPro Innovations for the alloy powders and the use of instruments and scientific and technical assistance at the Monash Centre for Additive Manufacturing (MCAM) and Monash Centre for Electron Microscopy (MCEM) as a Node of Microscopy Australia. S. Wu and H.Z. Peng wish to thank the financial support from the Monash Graduate Scholarship.

References

[1] R.C. Reed, Superalloy Fundamentals and Applications Book, 2006.
[2] M. Zhang, B. Zhang, Y. Wen, X. Qu, Research progress on selective laser melting processing for nickel-based superalloy, Int. J. Miner. Metall. Mater. 29 (2022) 369–388.
[3] D. Srinivasan, K. Ananth, Recent advances in alloy development for metal additive manufacturing in gas turbine/aerospace applications: a review, J. Indian Inst. Sci. (2022) 1–39.
[4] D. Herzog, V. Seyda, E. Wycisk, C. Emmelmann, Additive manufacturing of metals, Acta Mater. 117 (2016) 371–392.
[5] N. Khanna, K. Zadafiya, T. Patel, Y. Kaynak, R.A. Rahman Rashid, A. Vafadar, Review on machining of additively manufactured nickel and titanium alloys, J. Mater. Res. Technol. 15 (2021) 3192–3221.
[6] J.C. Najmon, S. Raeisi, A. Tovar, Review of Additive Manufacturing Technologies and Applications in the Aerospace Industry, Elsevier Inc., 2019.
[7] D. Tomus, P.A. Rometsch, M. Heilmaier, X. Wu, Effect of minor alloying elements on crack-formation characteristics of Hastelloy-X manufactured by selective laser melting, Addit. Manuf. 16 (2017) 65–72.
[8] B. Guo, Y. Zhang, Z. Yang, D. Cui, F. He, J. Li, Z. Wang, X. Lin, J. Wang, Cracking mechanism of Hastelloy X superalloy during directed energy deposition additive manufacturing, Addit. Manuf. 55 (2022), 102792.
[9] M.L. Montero-Sistiaga, Z. Liu, L. Bautmans, S. Nardone, G. Ji, J.P. Kruth, J. Van Humbeeck, K. Vanmeensel, Effect of temperature on the microstructure and tensile properties of micro-crack free hastelloy X produced by selective laser melting, Addit. Manuf. 31 (2020), 100995.
[10] Q. Han, Y. Gu, S. Soe, F. Lacan, R. Setchi, Effect of hot cracking on the mechanical properties of Hastelloy X superalloy fabricated by laser powder bed fusion additive manufacturing, Opt Laser. Technol. 124 (2020), 105984.
[11] R. Esmaeilizadeh, A. Keshavarzkermani, U. Ali, B. Behravesh, A. Bonakdar, H. Jahed, E. Toyserkani, On the effect of laser powder-bed fusion process parameters on quasi-static and fatigue behaviour of Hastelloy X: a microstructure/defect interaction study, Addit. Manuf. 38 (2021) 2214–8604.
[12] X. Zhang, H. Xu, Z. Li, A. Dong, D. Du, L. Lei, G. Zhang, D. Wang, G. Zhu, B. Sun, Effect of the scanning strategy on microstructure and mechanical anisotropy of Hastelloy X superalloy produced by Laser Powder Bed Fusion, Mater. Char. 173 (2021), 110951.
[13] O. Sanchez-Mata, X. Wang, J. Alberto Muñiz-Lerma, S.E. Atabay, M.A. Shandiz, M. Brochu, Dependence of mechanical properties on crystallographic orientation in nickel-based superalloy Hastelloy X fabricated by laser powder bed fusion, J. Alloys Compd. 865 (2021).
[14] S. Hibino, T. Todo, T. Ishimoto, O. Gokcekaya, Y. Koizumi, K. Igashira, T. Nakano, Control of crystallographic texture and mechanical properties of hastelloy-X via laser powder bed fusion, Crystals 11 (2021).
[15] X. Cheng, Y. Zhao, Z. Qian, J. Wu, J. Dong, Z. Ma, Y. Liu, Crack elimination and mechanical properties enhancement in additive manufactured Hastelloy X via in-situ chemical doping of Y2O3, Mater. Sci. Eng. 824 (2021).
[16] B. Diepold, M.S. Palm, A. Wimmer, T. Sebald, H.W. Höppel, S. Neumeier, M. Göken, Rotating scan strategy induced anisotropic microstructural and mechanical behavior of selective laser melted materials and their reduction by heat treatments, Adv. Eng. Mater. 23 (2021).
[17] B. Guo, Y. Zhang, F. He, J. Ma, J. Li, Z. Wang, J. Wang, J. Feng, W. Wang, L. Gao, Origins of the mechanical property heterogeneity in a hybrid additive manufactured Hastelloy X, Mater. Sci. Eng. 823 (2021), 141716.
[18] D. Tomus, Y. Tian, P.A. Rometsch, M. Heilmaier, X. Wu, Influence of post heat treatments on anisotropy of mechanical behaviour and microstructure of Hastelloy-X parts produced by selective laser melting, Mater. Sci. Eng. 667 (2016) 42–53.
[19] Y. Yin, J. Zhang, J. Gao, Z. Zhang, Q. Han, Z. Zan, Laser powder bed fusion of Ni-based Hastelloy X superalloy: microstructure, anisotropic mechanical properties and strengthening mechanisms, Mater. Sci. Eng. 827 (2021).

[20] D. Zhang, S. Wang, H. Zhang, C. Tan, Q. Gao, X. Liu, Z. Cui, Microstructure and mechanical properties of Hastelloy-X produced by selective laser melting, in: IOP Conference Series: Materials Science and Engineering, 2020.
[21] A.N. Jinoop, C.P. Paul, J. Ganesh Kumar, V. Anilkumar, R. Singh, S. Rao, K. S. Bindra, Influence of heat treatment on the microstructure evolution and elevated temperature mechanical properties of Hastelloy-X processed by laser directed energy deposition, J. Alloys Compd. 868 (2021).
[22] W. Zhang, Y. Zheng, F. Liu, D. Wang, F. Liu, C. Huang, Q. Li, X. Lin, W. Huang, Effect of solution temperature on the microstructure and mechanical properties of Hastelloy X superalloy fabricated by laser directed energy deposition, Mater. Sci. Eng. 820 (2021).
[23] J. Kangazian, M. Shamanian, A. Kermanpur, E. Foroozmehr, M. Badrossamay, Investigation of microstructure-tensile behavior relationship in Hastelloy X Ni-based superalloy processed by laser powder-bed fusion: insights into the elevated temperature ductility loss, Mater. Sci. Eng. 823 (2021).
[24] X. Cheng, Z. Du, S.X. Chu, J. Wu, J. Dong, H. Wang, Z. Ma, The effect of subsequent heating treatment on the microstructure and mechanical properties of additive manufactured Hastelloy X alloy, Mater. Char. 186 (2022), 111799.
[25] A. Shaji, D. Fraser, Y. Zhu, X. Wu, A. Huang, Effect of solution heat treatment and hot isostatic pressing on the microstructure and mechanical properties of Hastelloy X manufactured by electron b eam powder b e d fusion, J. Mater. Sci. Technol. 98 (2022) 99–117.
[26] A. Shaji, Y. Zhu, X. Wu, A. Huang, Microstructure, mechanical behaviour and strengthening mechanisms in Hastelloy X manufactured by electron beam and laser beam powder bed fusion, J. Alloys Compd. 862 (2021).
[27] E. De Bruycker, A. Gotti, E. Poggio, K. Boschmans, O. Tassa, A. Costa, A. Sanguineti, Short-term creep behaviour of additive manufactured Hastelloy X material, Mater. A. T. High. Temp. 00 (2022) 1–10.
[28] S. Wu, H.Y. Song, H.Z. Peng, P.D. Hodgson, H. Wang, X.H. Wu, Y.M. Zhu, M. C. Lam, A.J. Huang, A microstructure-based creep model for additively manufactured nickel-based superalloys, Acta Mater. 224 (2022), 117528.
[29] Y.L. Kuo, S. Horikawa, K. Kakehi, Effects of build direction and heat treatment on creep properties of Ni-base superalloy built up by additive manufacturing, Scripta Mater. 129 (2017) 74–78.
[30] J.J. Shi, X. Li, Z.X. Zhang, G.H. Cao, A.M. Russell, Z.J. Zhou, C.P. Li, G.F. Chen, Study on the microstructure and creep behavior of Inconel 718 superalloy fabricated by selective laser melting, Mater. Sci. Eng. 765 (2019), 138282.
[31] H.Y. Song, M.C. Lam, Y. Chen, S. Wu, P.D. Hodgson, X.H. Wu, Y.M. Zhu, A. J. Huang, Towards creep property improvement of selective laser melted Ni-based superalloy IN738LC, J. Mater. Sci. Technol. 112 (2021) 301–314.
[32] Z. Xu, L. Cao, Q. Zhu, C. Guo, X. Li, X. Hu, Z. Yu, Creep property of Inconel 718 superalloy produced by selective laser melting compared to forging, Mater. Sci. Eng. 794 (2020), 139947.
[33] M. Okugawa, D. Izumikawa, Y. Koizumi, Simulations of non-equilibrium and equilibrium segregation in nickel-based superalloy using modified scheil-gulliver and phase-field methods, Mater. Trans. 61 (2020) 2072–2078.
[34] H. Wang, L. Chen, B. Dovgyy, W. Xu, A. Sha, X. Li, H. Tang, Y. Liu, H. Wu, M.-S. Pham, Micro-cracking, microstructure and mechanical properties of Hastelloy-X alloy printed by laser powder bed fusion: as-built, annealed and hot-isostatic pressed, Addit. Manuf. 39 (2021), 101853.
[35] R.P. Baron, Creep and Stress-Rupture Failures, ASM Handbook, 2021, pp. 432–443.
[36] L. Damage, A. Rule, Prediction of creep-fatigue life, High Temp. Deform. Fract. Mater. (2010) 319–329.
[37] V. Norman, M. Calmunger, An accelerated creep assessment method based on inelastic strain partitioning and slow strain rate testing, Mater. Des. 205 (2021).
[38] Y. Estrin, Dislocation-density-related constitutive modeling, in: Unified Constitutive Laws of Plastic Deformation, Academic Press, INC., 1996, pp. 69–106.
[39] R.N. Stevens, Grain-boundary sliding in metals, Metall. Rev. 11 (1966) 129–142.
[40] T.G. Langdon, Grain boundary sliding revisited: developments in sliding over four decades, J. Mater. Sci. 41 (2006) 597–609.
[41] R.L. Bell, T.G. Langdon, An investigation of grain-boundary sliding during creep, J. Mater. Sci. 2 (1967) 313–323.
[42] K.L. Murty, S. Gollapudi, K. Ramaswamy, M.D. Mathew, I. Charit, Creep deformation of materials in light water reactors (LWRs), in: Materials Ageing and Degradation in Light Water Reactors: Mechanisms and Management, Woodhead Publishing Limited, 2013, pp. 81–148.
[43] A. Drexler, A. Fischersworring-Bunk, B. Oberwinkler, W. Ecker, H.P. Gänser, A microstructural based creep model applied to alloy 718, Int. J. Plast. 105 (2018) 62–73.
[44] T. Sugahara, K. Martinolli, D.A.P. Reis, C. Moura Neto, A.A. Couto, F. Piorino Neto, M.J.R. Barboza, Creep behavior of the inconel 718 superalloy, Defect Diffusion Forum 326–328 (2012) 509–514.
[45] M.C. Chaturvedi, Creep deformation of alloy 718, Inst. Aeronaut. Mater. 369 (1989) 1689–1699.
[46] S. Wu, H.Z. Peng, X. Gao, P.D. Hodgson, H.Y. Song, Y.M. Zhu, Y. Tian, A.J. Huang, Improving creep property of additively manufactured Inconel 718 through specifically-designed post heat treatments, Mater. Sci. Eng. 857 (2022), 144047.
[47] T.G. Langdon, An evaluation of the strain contributed by grain boundary sliding in superplasticity, Mater. Sci. Eng. 174 (1994) 225–230.
[48] W.Z. Rachinger, Relative grain translations in the plastic flow of aluminium, J. Inst. Met. 81 (1952) 33.
[49] R. Raj, M.F. Ashby, On grain boundary sliding and diffusional creep, Metall. Trans. A 2 (1971) 1113–1127.
[50] Y. Estrin, M. Heilmaier, G. Drew, Creep Properties of an Oxide Dispersion Strengthened Nickel-Base Alloy: the Effect of Grain Orientation and Grain Aspect Ratio, 1999.
[51] H.J. Frost, M.F. Ashby, Deformation-mechanism Maps : the Plasticity and Creep of Metals and Ceramics, Pergamon Press, 1982.
[52] R.L. Bell, C. Graeme-Barber, Surface and interior measurements of grain boundary sliding during creep, J. Mater. Sci. 5 (1970) 933–944.